Finite-strain, finite-size mechanics of rigidly cross-linked biopolymer networks

Stefan Lindström, Artem Kulachenko, Louise M. Jawerth and David A. Vader

Original Publication:

Stefan Lindström, Artem Kulachenko, Louise M. Jawerth and David A. Vader, Finite-strain, finite-size mechanics of rigidly cross-linked biopolymer networks, 2013, Soft Matter, (9), 30, 7302-7313.
http://dx.doi.org/10.1039/c3sm50451d

Finite-strain, finite-size mechanics of rigidly cross-linked biopolymer networks

Stefan B. Lindström,*[a] Artem Kulachenko[b], Louise M. Jawerth,[c] and David A. Vader[c]

The network geometries of rigidly cross-linked fibrin and collagen type I networks are imaged using confocal microscopy and characterized statistically. This statistical representation allows for the regeneration of large, three-dimensional biopolymer networks using an inverse method. Finite element analyses with beam networks are then used to investigate the large deformation, nonlinear elastic response of these artificial networks in isotropic stretching and simple shear. For simple shear, we investigate the differential bulk modulus, which displays three regimes: a linear elastic regime dominated by filament bending, a regime of strain-stiffening associated with a transition from filament bending to stretching, and a regime of weaker strain-stiffening at large deformations, governed by filament stretching convolved with the geometrical nonlinearity of the simple shear strain tensor. The differential bulk modulus exhibits a corresponding strain-stiffening, but reaches a distinct plateau at about $5\,\%$ strain under isotropic stretch conditions. The small-strain moduli, the bulk modulus in particular, show a significant size-dependence up to a network size of about 100 mesh sizes. The large-strain differential shear modulus and bulk modulus show very little size-dependence.

1 Introduction

Filamentous biopolymers self-assemble into stiff bundles, and form percolating networks through cross-linking or branching during polymerization.[1] Network-forming biopolymers are pervasive components in biological tissue. The cytoskeleton is composed of microtubules[2], intermediate filaments[3] and filamentous actin networks[2], fibrin polymerizes in wounds to form blood clots[4] and collagen constitutes the bulk of the extracellular matrix and the connective tissues[5]. Biopolymer networks display a remarkable range of mechanical properties; they can be extremely extensible[6,7] and exhibit strong strain-stiffening[6–9] to ensure cell and tissue integrity[8]. The mechanical characteristics of branched, athermal biopolymer networks derive from the individual strand behavior[10,11], the angle distribution between filaments[12], the number of branch-points per coherent fiber[13] and the network topology[14–16].

In this work, we study the finite-strain mechanical characteristics of reconstituted, cross-linked collagen type I and fibrin networks in the low-frequency limit. The networks we study have rigid branch-points and are athermal in the sense that the persistence length of the filaments exceeds the mesh size. Moreover, we only consider the linear-elastic regime of filament deformations. The range of this regime depends on the biopolymer species and the preparation process. Cross-linked fibrin filaments have a linear force–deformation relation up to $120\,\%$ elongation[17], and cross-linked collagen is linear to about $25\,\%$ elongation[18,19]. The microscopic mechanism behind these force-elongation characteristics is beyond the scope of this work.

Previous modeling work on the mechanics of disorganized fiber networks have been largely concerned with regular lattices with variable filament stiffness[20,21], random network geometries[12,14,16,22–26] and networks created through a simulated polymerization process[27]. An important generic result is that the hyperelastic response of low-connectivity networks is due to the excitation of nonaffine, bending-dominated modes of deformation at small strains, followed by a transition to stretching-dominated filament deformation at large network strains[12,13,20,23]. This mechanism for strain-stiffening is manifested at the macroscopic scale by an inflating differential shear modulus, observed in rheological experiments for collagen[6,9] as well as fibrin[7,9]. Also, the effects of nonlinear material characteristics of the strands have been previously modeled, including the effect of entropy of the polymer strands[28] and protein unfolding[29] in the case of fibrin. In this work, however, we focus on geometrical nonlinearities at large deformations.

To achieve a quantitative predictive capability of the large-deformation material characteristics, a detailed description of the network geometry is required[15,30], which is available through confocal microscopy[28,31]. It has been previously demonstrated, for one instance of a small collagen network, that the filament length distribution, the valency distribution and the distribution of direction cosines between filaments is sufficient for predicting the mechanical response to simple

[a] *Mechanics, Department of Management and Engineering, the Institute of Technology, Linköping University, SE-581 83 Linköping, Sweden. Fax: +46 13 149403; Tel: +46 13 281127; E-mail: stefan.lindstroem@gmail.com*

[b] *Department of Solid Mechanics, Royal Institute of Technology, SE-100 44 Stockholm, Sweden.*

[c] *School of Engineering and Applied Sciences, Harvard University, Cambridge, MA 02138, USA.*

shear deformations up to a shear strain of $\gamma = 0.3$[15]. Large deformations of individual filaments, including buckling, must also be taken into account. This can be achieved using a semi-flexible, worm-like chain model[16,28,30], or *e.g.* large deformation Timoshenko beam elements[15]. Such detailed models have been employed for the case of small, reconstituted collagen[15,30] and fibrin[28] networks. Knowing that the details of the geometry is accounted for and having a well-defined and very realistic model for large filament deformations enable us to address outstanding research questions specific to biopolymer networks:

a. Statistical network representation. Is it possible to describe the network geometry statistically while still capturing its mechanical characteristics? And if so, what are the similarities and differences between the network geometries of different biopolymer species?

b. Size-dependence. To what extent does network size affect the elastic mechanical response? The shear stiffness of thin collagen discs are known to be size-dependent[32], and finite-size behavior is key to understanding confined networks and boundary effects. The mechanisms behind these size-effects have not been previously addressed in the literature, to the knowledge of the authors.

c. Validity of the linear-elastic assumption for describing filaments. Can the nonlinear large deformation response of biopolymer networks be understood from the geometrical nonlinearity at the level of filaments and the finite strain nonlinearity of the bulk, using a linear-elastic beam model to represent the filaments? and what is the range of validity for this linear-elastic assumption for the filament material?

We use confocal microscopy to obtain three-dimensional micrographs of the biopolymer network structure[31], and characterize these structures statistically. Using an inverse method, these network statistics enable a numerical reconstruction of artificial networks of arbitrary size[15]. We numerically show that the physical and the artificial network structures are mechanically equivalent, in the sense that they exhibit the same large deformation mechanical response in simple shear and isotropic stretching. Finite-size effects are studied for artificial networks corresponding to collagen-I and fibrin network structures. We also separate the total strain energy into energies stored in the longitudinal, bending, torsional and transverse shear filament deformations to identify the governing microscale filament deformation mechanism. Importantly, we use state-of-the-art beam models implemented in commercially available finite element software to capture the filament-level geometrical nonlinearity, and the results are interpreted on the bulk level taking the nonlinearity of the strain tensor for simple shear and isotropic stretch into account.

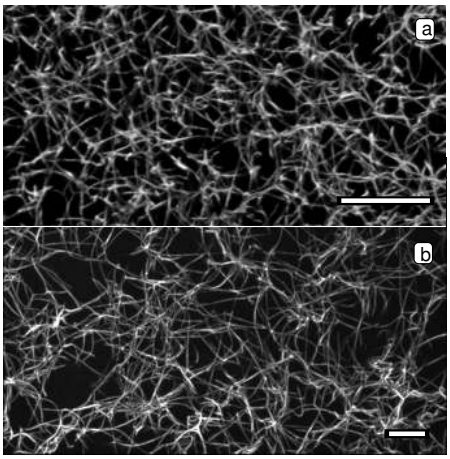

Fig. 1 (a) Confocal microscope image of a 1.0 g/L collagen network, with an image depth of 5 μm. (b) Confocal microscope image of a 0.4 g/L fibrin network, with an image depth of 28 μm. The scalebars are 20 μm.

2 Materials and methods

2.1 Experiments

We study isotropic, reconstituted networks of collagen type I (Fig. 1a) and fibrin (Fig. 1b). Bovine collagen type I is fluorescently labeled with tetramethylrhodamine isocyanate (TRITC), following a previously described protocol[33]. It is polymerized at final collagen concentrations 1.0, 2.0 and 4.0 g/L[34]. Fibrinogen is fluorescently labeled with TAMRA (c-1171 from invitrogen) and subsequently polymerized through the addition of thrombin, as previously described[35,36], at final fibrin concentrations of 0.4 and 1.6 g/L. The biopolymers are imaged in three dimensions using a Leica SP5 confocal microscope (Wetzlar, Germany) equipped with a 63×/1.2 NA water immersion lens, yielding voxel-based network representations with a width exceeding 30 mesh-sizes. The confocal microscope image stacks are converted into Euclidean graph representations using Amira's skeletonization package (TGS, San Diego, CA). The nodes of the graph represent branch-points, while the edges represent filaments[14,15,23,31]. The Euclidean graphs are subsequently analyzed for geometry statistics (Sec. 2.2).

For the mechanical characterization, collagen and fibrin gels are polymerized in a plate–plate geometry of an AR-G2 stress-controlled rheometer (TA Instruments, New Castle, DE). Strain ramps are used to measure the differential shear modulus as a function of shear strain in the low-frequency limit.

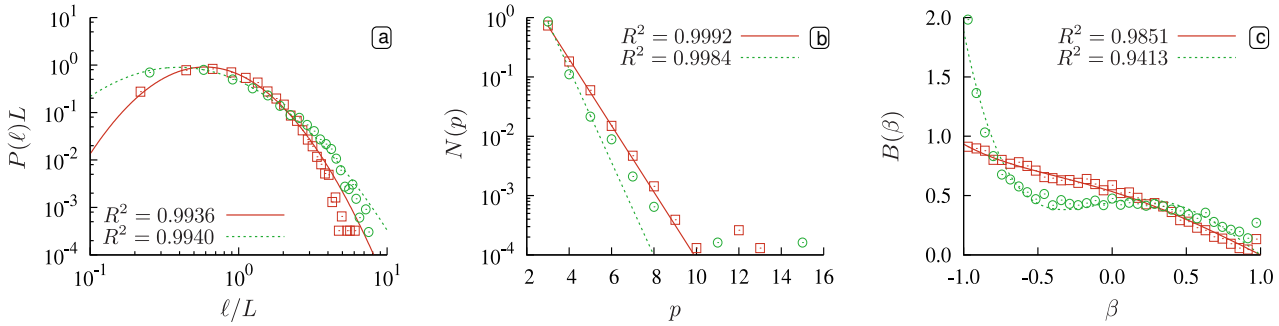

Fig. 2 Statistical description of the network geometry, where the analytical distributions are least-squares fitted in linear space. The Efron pseudo-R^2 value is provided for the fits. (a) Filament length distributions $P(\ell)$, normalized using the average filament length L, for a 1.0 g/L collagen network (squares, solid line) and a 0.4 g/L fibrin network (circles, dashed line). (b) Measured distribution $N(p)$ of valencies p and shifted geometric distributions. (c) Measured direction cosines distributions $B(\beta)$ and power series approximations.

2.2 Network characterization

A statistical network description has been previously proposed and shown to be sufficient for capturing the nonlinear elastic response of collagen-I[15]. This description includes (a) the filament length distribution $P(\ell)$, which enforces macroscale homogeneity by precluding too many short or long filaments. The filament length ℓ is taken as the edge length. (b) The valency distribution $N(p)$, which enforces the correct topology; the valency $p \in [3, \infty)$ is the number of incident edges to a node. (c) The direction cosines distribution $B(\beta)$, which is the probability density of cosines β between edges incident to the same node and enforces direction correlations within the network.

Experimentally, we observe that the fibrin and collagen networks have a log-normal filament length distribution $P(\ell)$ (Fig. 2a), although we make no claim that this is generally the case. We have

$$P(\ell) = \frac{1}{\ell\sqrt{2\pi\zeta^2}} \exp\left[-\frac{(\lambda - \ln \ell)^2}{2\zeta^2}\right], \qquad (1)$$

$$\zeta^2 = \ln\left(\frac{s^2}{L^2} + 1\right), \quad \lambda = \ln L - \frac{\zeta^2}{2},$$

where L and s^2 are the mean and variance of $P(\ell)$. We choose to parameterize the filament length distributions using the mean L and normalized variance $v = s^2/L^2$ of the filament length. This distribution is fit in linear space to experimental data from collagen and fibrin networks (Fig. 2a).

In fibrin and collagen networks alike, experiments indicate that $N(p)$ decreases exponentially with valency. We thus propose a shifted geometric distribution

$$N(p) = q(1-q)^{p-3}, \quad q = 1/(Z-2), \qquad (2)$$

with $Z = \sum_{p=3}^{\infty} pN(p)$ the coordination number. This distribution is fit in linear space to experimental data from collagen and fibrin networks, as shown in Fig. 2b. The discrepancy between the data points and the fit at the tail of the distribution is exaggerated due to the logarithmic plot.

The direction cosines distribution $B(\beta), \beta \in [-1, 1]$ does not take the shape of any standard distribution. The excluded volume of filaments ensures that $B(1) = 0$ for straight filaments. Therefore, we choose to approximate $B(\beta)$ using a truncated power series

$$B(\beta) = \sum_{k=1}^{m} b_k (1-\beta)^{2k-1}. \qquad (3)$$

Requiring that $\int_{-1}^{1} B(\beta)\mathrm{d}\beta = 1$ leaves $m-1$ independent parameters to be determined by data fitting. In this work, we choose $m = 3$. Measured direction cosines distributions from fibrin (0.4 g/L) and collagen (1.0 g/L) are plotted with corresponding fitted distributions in Fig. 2c. The maximum of B is located at $\beta = -1$, for all biopolymers. This maximum $\hat{B} = B(-1)$ is a manifestation of cross-linking between longer, straight fibers and the corresponding increase in the direction correlation of incident filaments. The peak at $\beta = 1$ represents the case when two filaments connect the same pair of nodes; such loops are permissible for non-straight filaments, but neglected in this proposed statistical description.

Five independent parameters L, v, Z, b_1 and $\hat{B}$ are thus needed for the statistical description of the network geometry. These parameters are compiled in Table 1 for different biopolymer species and monomer concentrations. In this limited data set, the normalized variance is particular to the species: $v \approx 0.34$ for fibrin and $v \approx 0.25$ for collagen. The coordination number of the networks is in the range $3.19 < Z < 3.44$, where fibrin has a slightly lower connectivity than collagen. The fact that $\hat{B}$ is greater for fibrin than for collagen, shows that fibrin tends to form more coherent fibers, extending over several mesh sizes.

Table 1 Measured parameters of the network statistics for different biopolymer species and monomer concentrations.

	conc. [g/L]	L [μm]	v [-]	Z [-]	b_1 [-]	$\hat{B}$ [-]
fibrin	0.4	4.87	0.339	3.19	0.94	1.89
≀	1.6	2.99	0.341	3.33	0.91	1.51
collagen-I	1.0	1.96	0.253	3.38	0.62	0.93
≀	2.0	1.81	0.247	3.44	0.67	0.91
≀	4.0	1.28	0.256	3.41	0.74	1.13

From the network geometry parameters, networks can be generated using the Euclidean Graph Generation (EGG) algorithm[15], an inverse method using simulated annealing to create artificial networks arbitrarily close to the target statistics. In this work, the EGG algorithm is slightly modified to enhance its performance for very large networks*.

The stretching modulus μ, flexural rigidity κ and diameter D of individual fibrin and collagen filaments are found in the literature, or computed from data found in the literature[17,34]; no fitting procedure is employed to obtain the filament properties. For collagen, the average flexural rigidity and filament width was previously measured[34]. For fibrin, the average tensile stiffness and filament width is available.[17] The elastic modulus of the filaments E_f is computed for both biopolymer species by assuming that the filament cross-section is circular. The reader should be aware this latter assumption introduces an error in the computed stretching modulus of collagen and computed flexural rigidity of fibrin. We conservatively claim to achieve an order-of-magnitude estimate for the stiffness parameters. These are compiled in Table 2, including the persistence length $\ell_\mathrm{p} = \kappa/k_\mathrm{B}T$ to show that the filaments are athermal. The Poisson's ratio of the materials comprising the filaments is taken to be $\nu = 0.3$. As previously demonstrated experimentally, cross-linked fibrin filaments have a linear force–deformation relation up to 120 % elongation[17], and cross-linked collagen is linear to about 25 % elongation[18,19]. We limit the scope of our investigation to this linear regime of filament deformations, understanding that it is straight-forward to extend the model to the nonlinear material behavior observed at vary large strain of fibrin and collagen filaments.

The magnitude of the shear modulus G of entropic networks is $k_\mathrm{B}T/L^3$. For athermal networks, the shear modulus becomes κ/L^4 when filaments deform mainly in bending and μ/L^2 for isostatic networks when deformations are dominated by stretching. We assess which is the dominant mode of deformation by comparing the measured shear modulus with these magnitude estimates (Table 3). It is observed that $k_\mathrm{B}T/L^3 \ll G$ for all networks, confirming that they are athermal. Moreover, since $\mu/L^2 \gg G$ for all networks considered, filament bending is the dominant deformation mechanism for infinitesimal strains. This is consistent with the fact that these networks have a coordination number below that of Maxwell's isostatic connectivity threshold, *i.e.* $Z < 6$ (Table 1) for three-dimensional networks[37,38]. That is to say, the number of internal degrees of freedom of the network is greater than the number of constraints originating from central-force interactions. If there is a bending to stretching transition at finite strains, as previously proposed[20], this transition could potentially stiffen the networks by a factor $\mu L^2/\kappa$; that is by a factor 10^3 to 10^4 for the networks listed in Table 3.

* An additional term $|\langle\ell\rangle/L - 1|$, with $\langle\cdot\rangle$ the ensemble average, is added to the energy function in Ref. 15 to penalize very long fibers.

Table 2 Stiffness parameters of fibrin and collagen filaments. Literature values are used where indicated. The other parameters are computed using linear elastic beam theory.

	D [μm]	E_f [MPa]	κ [10^{-21} Nm^2]	μ [μN]	ℓ_p [cm]
fibrin	0.39[a]	4.0[a]	4.5	0.48	110
collagen-I	0.10[b]	100	0.5[b]	0.80	12

[a] Liu et al.[17].
[b] Vader[34].

Table 3 Measured and predicted magnitudes of the shear modulus.

	conc. [g/L]	G [Pa]	$k_\mathrm{B}T/L^3$ [Pa]	κ/L^4 [Pa]	μ/L^2 [Pa]
fibrin	0.4	1.2	0.00004	0.89	$2.0{\cdot}10^4$
≀	1.6	40	0.0002	6.3	$5.3{\cdot}10^4$
collagen-I	1.0	24	0.005	34	$2.1{\cdot}10^5$

2.3 Simulation geometry and deformations

A Cartesian coordinate frame with base vectors $\{\hat{\boldsymbol{e}}_1, \hat{\boldsymbol{e}}_2, \hat{\boldsymbol{e}}_3\}$ is introduced. For simple shear deformation (Fig. 3a), investigated to obtain the differential shear modulus, the components of the average displacement field $\boldsymbol{u}(\boldsymbol{x})$ are given by

$$u_1 = \gamma x_2, \quad u_2 = 0, \quad u_3 = 0, \tag{4}$$

where $\boldsymbol{x}$ is the position vector of a material point in the undeformed state and γ is the applied shear. In the case of isotropic stretching (Fig. 3b), studied to obtain the differential bulk modulus, the average displacement field is

$$u_i = (\lambda - 1)x_i, \quad i = 1, 2, 3, \tag{5}$$

where λ is the stretch, and $\lambda = 1$ corresponds to an undeformed sample.

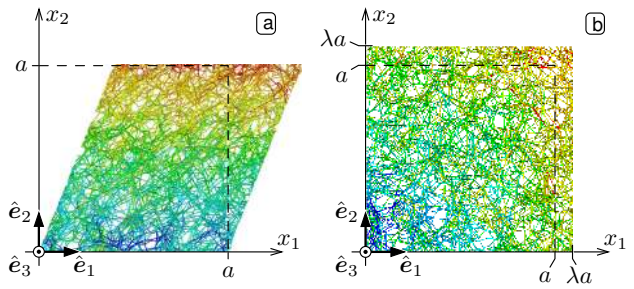

Fig. 3 Projections of three-dimensional network deformations for a cubic, regenerated 1.0 g/L collagen network of width $a = 20L$. The color (online) represents displacement: blue is zero; red is maximum. (a) The gradient plane at 40 % shear. (b) The x_1x_2 plane at 10 % isotropic stretch, *i.e.* in all three directions.

We define the differential shear and bulk moduli, respectively, as

$$\mathcal{G}(\gamma) = \frac{\mathrm{d}\tau_{12}}{\mathrm{d}\gamma}, \quad \mathcal{K}(\lambda) = -\frac{1}{3}\frac{\mathrm{d}p}{\mathrm{d}\lambda},$$

where τ_{ij} is the first Piola–Kirchhoff stress tensor and $p = -\tau_{\alpha\alpha}/3$ is the pressure. The shear and bulk moduli of infinitesimal deformations become

$$G = \mathcal{G}(0), \quad K = \mathcal{K}(1).$$

Simulations are conducted in a cubic domain of side length a aligned with the axes of the chosen coordinate frame. Each one of the six boundary planes is denoted by $S_{\hat{\boldsymbol{n}}}$, where $\hat{\boldsymbol{n}}$ is the outward unit normal. The networks are cropped at these boundaries, and the cut filament ends become boundary nodes. Simple shear or isotropic stretch is enforced by displacing these boundary nodes. The apparent material characteristics of the finite-size networks depend on the boundary node constraints applied to achieve the macroscopic deformation.

Boundary conditions are chosen to create deformations similar to those of the bulk of a large network. The physical networks are not periodic, prohibiting the use of periodic boundary conditions. Moreover, employing free boundary conditions at the $S_{\pm\hat{\boldsymbol{e}}_2}$ boundaries creates a necking effect and a stress-band along the diagonal of the sample in simple shear. Due to these considerations, two types of boundary conditions are employed herein: with determinate boundary conditions (DBC), all boundary nodes are subjected to a prescribed displacement according to Eq. (4) for simple shear or Eq. (5) for isotropic stretch, while being allowed to rotate freely. With indeterminate boundary conditions (IBC), simple shear is achieved by applying

$$\begin{aligned} u_1 &= \gamma x_2 \text{ on } S_{\pm\hat{\boldsymbol{e}}_1} \text{ and } S_{\pm\hat{\boldsymbol{e}}_2} \\ u_2 &= 0 \quad \text{on } S_{\pm\hat{\boldsymbol{e}}_1} \text{ and } S_{\pm\hat{\boldsymbol{e}}_2} \\ u_3 &= 0 \quad \text{on } S_{\pm\hat{\boldsymbol{e}}_3}. \end{aligned}$$

For isotropic stretch, we apply

$$u_i = (\lambda - 1)x_i \text{ on } S_{\pm\hat{\boldsymbol{e}}_i} \text{ for } i = 1, 2, 3.$$

Note that with IBC, the nodes are allowed to move freely in the lateral directions of the boundary planes. While DBC correspond to the network being anchored to surrounding membranes, IBC may better represent the conditions in the interior of a very large networks, as demonstrated in later Sec. 3.2.

For each simulation, $\gamma \in [0, 2.0]$ or $\lambda \in [1.0, 1.2]$ is increased linearly, in small steps, from the undeformed state to some target deformation. The stress tensor τ_{ij} is obtained by integrating the total node force on the boundary planes of the simulation domain at each step, and dividing by the original area.

2.4 Finite element model

We perform numerical simulations for simple shear and isotropic stretch of regenerated and physical network geometries, using a commercial, implicit time integration finite element code (ANSYS[39]). Since the filaments are reasonably slender, a beam theory is employed to model their mechanics. We test two classes of beam elements, representing the Timoshenko beam theory and a modified Euler beam theory augmented with a transverse shear effect. In the case of Timoshenko beam theory, the filaments are meshed with a 3-node quadratic beam element (`BEAM189` in ANSYS). In the case of modified Euler beam theory, we use a 2-node beam element (`BEAM4` in ANSYS) as well as a custom beam element programmed and linked through a user-element interface. All these elements are able to account for linearly varying bending moments, large rotations and large deformations. In the filament network, the beams are connected through the nodes at the branch-points, which ensures rigid translational and rotational connections between the filaments.

The custom beam element and `BEAM4` are identical in the sense that they both implement the same stiffness matrix. Both are derived from the engineering theory of bending, which—although being based on the classical Euler beam theory—accounts for the transverse shear forces[40]. Linearly varying longitudinal displacement is assumed within the element and cubic Hermite polynomials are used for transverse displacements. The calculations are performed in the local element coordinate system after the finite rotation transformation[41]. We use a projector-consistent stress–stiffness matrix[42,43] to achieve a quadratic rate of convergence.

The custom beam element is implemented for two reasons. The first reason is to compute the fractions of longitudinal, bending, torsional and shear energy of the total elastic energy stored in the network, as described in Appendix A. The partition of strain energy is investigated in later Sec. 3.3. The second reason is a more time-efficient implementation, achieved

by using an elastic, constant-temperature, pre-integrated beam that does not require any history variables to be passed between the Newton–Raphson iterations performed at each substep. Otherwise, history variables are required by the BEAM4 implementation to, for instance, store the temperature history.

3 Results

3.1 Discretization and integration

The filaments are modeled as chains of aligned, rigidly interconnected beam elements. The resolution or the mesh density is controlled by setting a maximum length L/N_{div} for the beam elements, where N_{div} is a numerical parameter. The differential shear modulus of artificial, 1.0 g/L collagen network is obtained by simulating simple shear using modified Euler beam elements and different discretizations $N_{\mathrm{div}} \in (0, 10]$, with IBC (Fig. 4a). Here and in the following, each simulation is repeated for three different network realizations. The resolution has very little effect on the prediction of the elastic response; these variations are much smaller than the variability between network realizations. Without any subdivision of the filaments, the simulations are terminated at $\gamma_{\max} \approx 0.4$. At this point, the implicit solution scheme fails due to divergence. By increasing the number of subdivisions, this limiting shear strain can be increased to $\gamma_{\max} > 1.0$ for $N_{\mathrm{div}} = 2.5$. Further refinement does not improve the performance in this respect.

For the same type of network and boundary conditions with $N_{\mathrm{div}} = 5$, we compare the differential shear modulus integrated using Timoshenko and modified Euler beam elements, respectively (Fig. 4b). The simulations using Timoshenko and modified Euler elements differ very little as compared to the difference between statistical realizations. It is also shown in Fig. 4b that the custom beam implementation produces results consistent with the BEAM4 implementation in ANSYS.

We conclude that the custom, pre-integrated Euler beam element captures the mechanics with sufficient accuracy, and that an almost optimal beam element length, in terms of computational speed and attained level of strain, is obtained using $N_{\mathrm{div}} = 3$ (Fig. 4a, inset). The remaining simulations are performed using custom Euler beam elements with $N_{\mathrm{div}} = 3$.

3.2 Finite-size dependence

To explore the finite-size dependence of biopolymer networks, we first consider artificial, 1.0 g/L collagen networks, and conduct numerical simulations to obtain $\mathcal{G}(\gamma)$ and $\mathcal{K}(\lambda)$ for different network sizes $a/L \in \{5, 10, 20, 40, 80\}$ with either DBC or IBC.

For all network sizes, the mechanical response in simple shear is similar. At least three regimes of elastic deformations

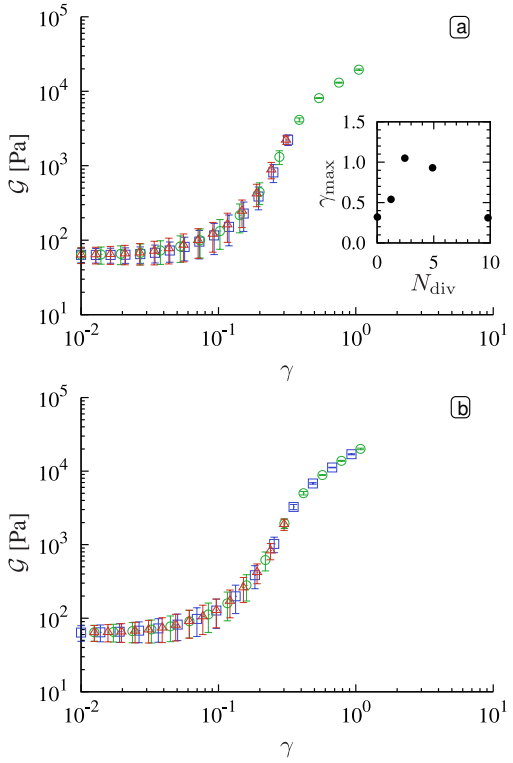

Fig. 4 Differential shear modulus of artificial, 1.0 g/L collagen networks, $a/L = 40$ with IBC. The error bars represent variability between statistical realizations. (a) Simulations using custom Euler beam elements with different resolution: no limit (squares), $N_{\mathrm{div}} = 2.5$ (circles), $N_{\mathrm{div}} = 10$ (up-triangles). The inset shows how the maximum strain $\gamma_{\max}$, captured by the simulations, changes with resolution. (b) Simulations with $N_{\mathrm{div}} = 5$ using custom Euler beam elements (squares), ANSYS Euler beam elements, BEAM4 (circles) and Timoshenko beam elements, BEAM189 (triangles).

can be identified (Fig. 5a): At relatively small strains, $\gamma < 0.1$, the response is linear elastic, as indicated by essentially constant $\mathcal{G}$. In the range $0.1 < \gamma < 0.4$, the network is strain-stiffening at an increasing rate. Finally, for $\gamma > 0.4$, the strain-stiffening proceeds at a somewhat slower rate, without reaching any distinct plateau before simulations are terminated at about $\gamma = 1.5$ strain due to divergence. The three regimes are consistent with experimentally observed mechanical response for highly extensible filaments, including collagen[6] and fibrin[7], and the strain-stiffening is usually attributed to a transition from bending-dominated to stretching-dominated modes of filament deformations[21]. According to Table 3, the theoretical upper limit of $\mathcal{G}$ is in the order of 10^5 Pa, which is not reached in the simulations, indicating that the strain-stiffening in simple shear could proceed even when $\gamma \gg 1$.

For each network size, the differential shear modulus of simulations with DBC is always greater than that of IBC

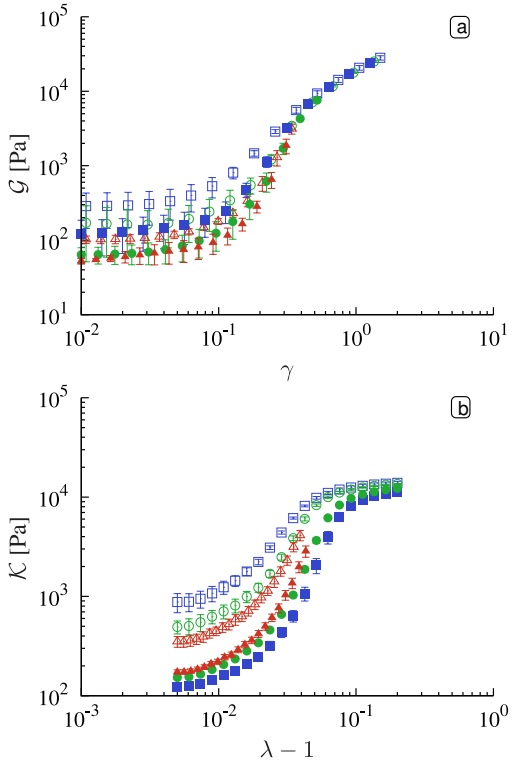

Fig. 5 Finite-strain material characteristics of artificial, 1.0 g/L collagen networks of different network sizes $a/L = 20$ (squares), $a/L = 40$ (circles) and $a/L = 80$ (triangles). Open symbols represent DBC and filled symbols IBC.

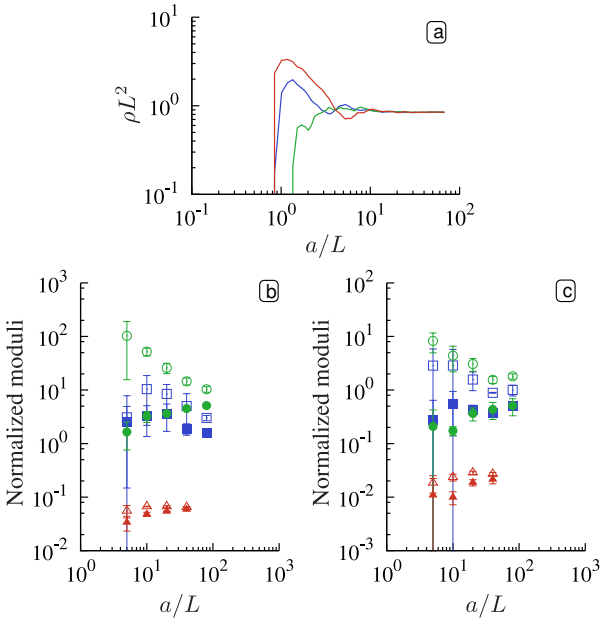

Fig. 6 (a) Computed density for finite-size domains of three different 1.0 g/L collagen network realizations. (b) Normalized moduli of 1.0 g/L collagen network realizations for different domain sizes; shear modulus GL^4/κ (squares), bulk modulus KL^4/κ (circles) and large-strain differential bulk modulus $\mathcal{K}_\infty L^2/\mu$ (triangles). Open symbols represent DBC and filled symbols IBC. (c) Normalized moduli of 0.4 g/L fibrin network realizations, with the same point representations as in (b).

(Fig. 5a). This is explained by the additional displacement constraints imposed by DBC. This difference between DBC and IBC is reduced for larger networks, presumably because the number of boundary constraints per unit volume diminishes. A reduction of the shear modulus G is seen for larger networks, which is also rationalized by the reduction of boundary constraints per unit volume. Interestingly, for large strain, $\gamma \gtrsim 0.40$, neither network size nor the type of boundary conditions affect $\mathcal{G}$ (Fig. 5a).

The differential bulk modulus $\mathcal{K}(\lambda)$ displays three regimes in the stretch λ (Fig. 5b): For very little stretch, $\lambda - 1 < 0.005$, the network is linear elastic, as manifested by an almost constant $\mathcal{K}$. Then, there is a regime of strain-stiffening in the approximate range $0.005 < \lambda - 1 < 0.05$. Finally, a distinct plateau in $\mathcal{K}$ is reached. The behavior is in qualitative agreement with the recently reported nonlinear mean-field-theory for disordered networks[44].

The DBC and IBC curve families of the differential bulk modulus show a size-dependent bulk modulus K (Fig. 5b). The DBC yield an overestimate of $\mathcal{K}(\lambda)$, while IBC yield an underestimate. The DBC and IBC curve families converge toward the bulk mechanical response of the network as the domain size increases. The differential bulk modulus ultimately reaches a plateau $\mathcal{K}_\infty$ that does not show any significant size-dependence.

To investigate at which size a homogenization of the biopolymer material is possible, we seek the Representative Elementary Volume (REV) for stress in simple shear and isotropic stretch, respectively. This investigation is limited to the collagen (1.0 g/L) and the fibrin (0.4 g/L) networks; the microstructures of these examples differ significantly in terms of coordination number and direction cosines distribution (Table 1). The density REV sets a lower bound on the REV of any density-dependent property. We thus investigate the length density ρ as a function of the size a/L of a control volume for different network realizations. The variability of the normalized length density ρL^2 diminishes as a/L increases, and the density REV is about $a/L = 10$ for collagen (Fig. 6a) and fibrin (not shown).

The size of the REV depends on the mechanical property we consider and on the boundary conditions, DBC or IBC, we apply. The simulated shear and bulk moduli, G and K, as well as the large-stretch differential bulk modulus $\mathcal{K}_\infty$ are plotted as functions of a/L for 1.0 g/L collagen (Fig. 6b) and for 0.4 g/L

fibrin (Fig. 6c). The infinitesimal strain characteristics depend on sample size and boundary conditions.

For 1.0 g/L collagen and DBC, corresponding to a network firmly anchored to surrounding boundaries, the bulk and shear moduli decreases by an order of magnitude from $a/L = 5$ to $a/L = 80$, approaching $K \approx 10\kappa/L^4$ for the largest networks (Fig. 6b). Conversely, relaxing the constraints on the boundary nodes using IBC, the bulk modulus increases with the network size, so that DBC and IBC gives an upper and a lower bound, respectively, for the mechanical properties of an infinitely large network. The large-stain differential bulk modulus $\mathcal{K}_\infty$ does not show any dependence on network size or boundary conditions. The relatively small value for $\mathcal{K}_\infty \approx 0.06\mu/L^2$ shows that only a fraction of the filaments become loaded in tension at the plateau. To accurately capture the material behavior in a general deformation, it is a necessary condition that both $\mathcal{G}(\gamma)$ and $\mathcal{K}(\lambda)$ is captured, so the size of the stress REV for the collagen network is about $a/L = 100$ (Fig. 6b).

In the case of 0.4 g/L fibrin (Fig. 6c), the situation is similar to that of the collagen network. Again, DBC and IBC simulations give upper and lower bounds for the bulk mechanical response. The normalized bulk modulus is almost ten times lower than that of the collagen network. This reduced normalized bulk modulus may be due to a smaller coordination number for fibrin (Table 1), which has been previously demonstrated to reduce the network stiffness [15].

3.3 Filament deformations

We reconsider the shear strain and isotropic stretch data of 1.0 g/L collagen, now focusing on the partition of strain energy between different modes of filament deformation; the different types of strain energies of the custom beam element are defined in Appendix A. Let the index k enumerate the four modes of filament deformation: longitudinal, bending, torsion and transverse shear. We define ψ_k to be the strain energy density associated with deformation type k. The total strain energy density of a linear elastic, isotropic material is given by [45]

$$\psi = \left(\frac{1}{2}K - \frac{1}{3}G\right)(e_{\alpha\alpha})^2 + Ge_{ij}e_{ij}, \tag{6}$$

with e_{ij} the components of the Euler–Almansi strain tensor $\mathbf{e}$.

For simple shear deformation, the Euler–Almansi finite strain tensor is [45]

$$\mathbf{e}_{\mathrm{ss}} = \frac{1}{2}\begin{bmatrix} 0 & \gamma & 0 \\ \gamma & -\gamma^2 & 0 \\ 0 & 0 & 0 \end{bmatrix}. \tag{7}$$

Inserting $\mathbf{e}_{\mathrm{ss}}$ into Eq. (6) yields the total strain energy density expected for a linear-elastic, isotropic material in simple shear:

$$\psi_{\mathrm{ss}}(\gamma) = \frac{1}{2}G\gamma^2 + \left(\frac{1}{6}G + \frac{1}{8}K\right)\gamma^4.$$

Consequently, the differential shear modulus $\mathcal{G} = \mathrm{d}^2\psi/\mathrm{d}\gamma^2$ of linear elastic materials always exhibits strain-stiffening due to the biquadratic term of ψ_{ss} associated with finite strain nonlinearity. To separate the finite strain bulk nonlinearity from the filament-level geometrical nonlinearity, it is of interest to investigate whether biopolymers strain-stiffen in excess of a linear-elastic material. Therefore, we study the normalized strain energy density $\psi_k(\gamma)/\psi_{\mathrm{ss}}(\gamma)$ for each type of filament deformation k.

Since the transition from the bending-dominated to the stretching-dominated regime of filament deformations is of particular interest, we use a network size, $a/L = 40$, somewhat smaller than the REV in these simulations; the numerical scheme fails to converge at a relatively early stage ($\gamma \approx 0.4$) for $a/L = 80$. The mechanical response is still qualitatively reproduced for $a/L = 40$, as shown in Fig. 5. The different types of strain energy is plotted for an artificial, 1.0 g/L collagen network in Fig. 7a. Bending strain energy dominates the initial material response. The initial strain-stiffening is associated with an increase in all types of strain energy; of which bending energy is still dominant. The energy due to stretching starts to dominate the mechanics at about $\gamma = 0.37$. At this point the strain energy increases rapidly and plateaus at about $\gamma = 1.0$. The fact that the normalized strain energy density reaches a plateau shows that the material behavior is similar to that of a linear elastic solid, $\psi \propto \gamma^4$, for large strains. Importantly, this means that the absence of a plateau in simulated $\mathcal{G}$ at large strains $\gamma \gtrsim 1.0$ for both collagen and fibrin (Fig 9ab) is due to finite strain bulk nonlinearity, not to inflation of the moduli of the biopolymer network.

For isotropic stretch, the Euler–Almansi strain tensor becomes [45]

$$\mathbf{e}_{\mathrm{is}} = \frac{\lambda^2 - 1}{2\lambda^2}\begin{bmatrix} 1 & 0 & 0 \\ 0 & 1 & 0 \\ 0 & 0 & 1 \end{bmatrix}. \tag{8}$$

We insert $\mathbf{e}_{\mathrm{is}}$ into Eq. (6) to obtain the total strain energy density of a linear elastic, isotropic material:

$$\psi_{\mathrm{is}}(\lambda) = \frac{9(\lambda^2 - 1)^2 K}{8\lambda^4}.$$

The normalized strain energy density $\psi_k(\lambda)/\psi_{\mathrm{is}}(\lambda)$ for each type of filament deformation k for isotropic stretching of the collagen network is plotted in Fig. 7b. Similarly to the case of simple shear, the initial strain-stiffening is dominated by filament bending until the point of equipartition of bending and stretching energy at $\lambda - 1 \approx 0.05$.

We consider the distribution of beam element nominal elongational strain ϵ_{n}, defined as $\epsilon_{\mathrm{n}} = \sigma_\ell/E_{\mathrm{f}}$, where σ_ℓ is the

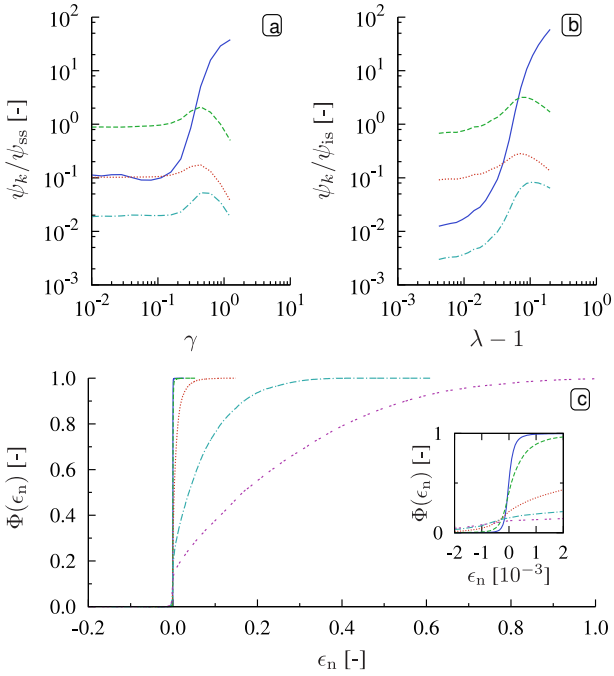

Fig. 7 (a) Normalized strain energy density of different modes of filament deformation for the artificial, 1.0 g/L collagen network in simple shear: tension (solid), bending (dashed), torsion (dotted) and transverse shear (dash-dotted). (b) The same strain energy partition for isotropic stretch. (c) The cumulative distribution function of the nominal tensile strain of the beams for the artificial, 1.0 g/L collagen network in simple shear. The curves correspond to different levels of shear strain: $\gamma = 0.1$ (solid), $\gamma = 0.2$ (dashed), $\gamma = 0.4$ (dotted), $\gamma = 0.8$ (dash-dotted) and $\gamma = 1.6$ (double-dashed).

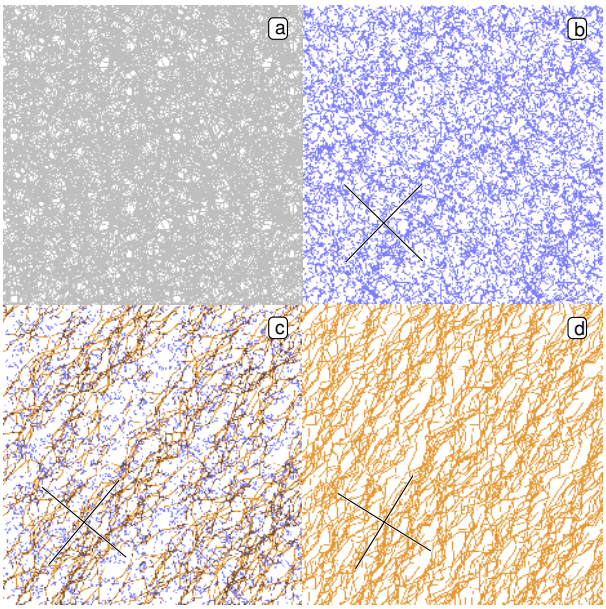

Fig. 8 Plots of the undeformed geometry of an artificial 1.0 g/L collagen network ($a/L = 40$). The cross-hairs indicate the principal directions of the Almansi strain tensor. (a) The full network. (b) The 20 % fraction of beam elements with the highest bending strain energy at $\gamma = 0.05$. (c) The 10 % fraction of beam elements with the highest bending strain energy, and the 10 % fraction of beam elements with the highest elongational strain energy at the point of strain energy equipartition, $\gamma = 0.37$. (d) The 20 % fraction of beam elements with the highest elongational strain energy at $\gamma = 1.0$.

nominal axial stress. The cumulative distribution function (CDF) of nominal strain $\Phi(\epsilon_n)$ of the beams of the network is plotted for the artificial 1.0 g/L collagen network for $\gamma \in \{0.1, 0.2, 0.4, 0.8, 1.6\}$ in Fig. 7c. The CDF of nominal strain is symmetric for low levels of shear strain, but becomes increasingly asymmetric as the shear strain increases. That is, at small shear strains, the filaments carry load in both tension and compression, whereas at high shear strain the filaments mainly carry load in tension. At the highest recorded shear strain $\gamma = 1.6$, most beams, 88 %, are loaded in tension. At a shear strain of $\gamma = 0.8$, essentially all filaments are elongated less than 25 %, which is within the linear force–deformation regime of cross-linked collagen[18,19]. That is, the network structure effectively promotes load-sharing among the fibers and ensures that no single fiber is subjected to an extreme load.

A projection of the artificial 1.0 g/L collagen network ($a/L = 40$) is depicted in Fig. 8a in its undeformed state. The spatial distribution and orientation distribution of the strain energy in the network are qualitatively studied by plotting the 20 % fraction of beam elements storing the greatest strain energy on the undeformed geometry. In the bending-dominated regime, exemplified by $\gamma = 0.05$ (Fig. 8b), the strain energy is randomly distributed across the network without any direction correlation with the principal strain directions, indicated by the cross-hair. The principal strain directions in the undeformed geometry are the eigendirections of the Euler–Almansi finite strain tensor, and correspond to removing rigid body rotation from the principal directions of the deformed geometry. In the stretching-dominated regime, here represented by $\gamma = 1.0$ (Fig. 8d), the strain energy is localized to filaments that are oriented in the tensile principal strain direction. For $\gamma = 0.37$, the strain energy of bending and stretching deformations are equal. At this point of strain energy equipartition, bending strain energy is uniformly distributed across the network, seemingly without any preferred direction. Elongational strain energy is localized in bands which are oriented in the tensile principal strain direction. This indicates the formation of shear bands in the structure.

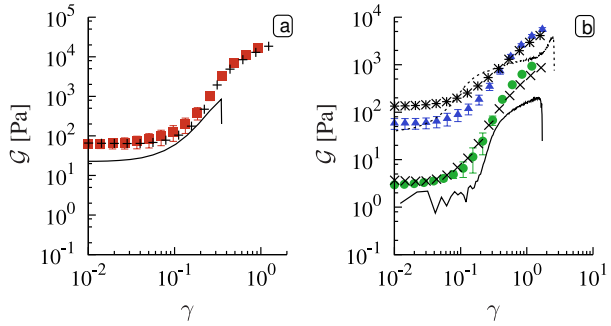

Fig. 9 (a) Differential shear modulus of 1.0 g/L collagen from simulations of regenerated networks using IBC (squares), simulations of physical network using IBC (+) and rheology (solid line). (b) Differential shear modulus of fibrin (0.4 g/L and 1.6 g/L), from regenerated networks using IBC (circles/triangles), physical network using IBC ($\times$/$*$) and rheology (solid/dashed line).

3.4 Comparing physical and artificial networks

Two questions arise regarding the validity of the proposed model: First, does the EGG algorithm capture the salient features of the network geometry to reproduce its mechanical response? Secondly, does the beam network model accurately capture the experimentally observed mechanical response? We address these questions by first comparing the simulated simple shear response of regenerated and physical network geometries, and then comparing the simulated response of regenerated networks with rheological measurements.

The physical network geometries, used above for network characterization, are cropped and subjected to simple shear FEM simulations using IBC, which captures the macroscale mechanical response of very large networks slightly better than DBC (Fig. 5a). The simulated differential shear modulus $\mathcal{G}(\gamma)$ of the regenerated networks is in quantitative agreement with that of the physical network geometries for collagen (Fig. 9a) as well as fibrin (Fig. 9b). This result is obtained without any fitting procedure. This confirms that the network characterization and regeneration successfully capture the network geometry.

Knowing now that the network geometries are correctly reproduced, we proceed to investigate the FEM model by comparing simulation results with rheometer measurements. We use the domain size $a/L = 40$ for these simulations, which is sufficient for capturing the shear modulus (Fig. 6bc). Note that all parameters of the network and constituents are obtained experimentally, so that no fitting procedure is involved.

For collagen (1.0 g/L), the simulated finite strain response is in fair agreement to the point of yielding at about $\gamma = 0.3$ (Fig. 9a). The discrepancy between experiment and simulations is likely due to the uncertainty associated with determining the collagen filament diameter and elastic modulus, and possibly the presence of a macroscopic concentration gradient in the polymerized network across sample, from the top plate of the rheometer holding the sample to the bottom plate.

In the case of 0.4 g/L fibrin, the simulated finite strain response up to about $\gamma = 0.3$ is again in a fair agreement with experiments, considering the uncertainty associated with the mechanical properties of the fibrin filaments. At very large deformations, $\gamma > 0.3$, the physical network displays a weaker strain-stiffening than the artificial network. Because the tensile force–deformation relation of cross-linked fibrin filaments is linear up 120 % elongation [17], the weaker strain-stiffening found in the experiments suggests inelastic material behavior at very large network deformations, which is beyond the scope of the present investigation.

For the higher-concentration 1.6 g/L fibrin network the shear modulus is predicted reasonably well for infinitesimal strains. However, at finite strains, the simulation results are not in qualitative agreement with experiments; strain-stiffening is initiated at $\gamma \approx 0.1$ in simulations, but already at $\gamma \approx 0.02$ in the experiments. Repeating the simulations for a larger network size, $a/L = 80$ (not shown), does not significantly affect the critical strain of strain-stiffening. It has been experimentally shown elsewhere that the rate-dependence of these cross-linked fibrin networks is very small at the low frequencies used herein [7], asserting that viscous effects could not be responsible for the premature strain-stiffening. Also, given the linear force-deformation relation of fibrin filaments [17], the effect is not due to material nonlinearity. One hypothesis, that will be investigated elsewhere, is that a concentration gradient across the sample, between the plates of the rheometer, yields an apparent early strain-stiffening, but this is not within the scope of this study.

4 Discussion

4.1 Network structures

The salient features of athermal biopolymer network structures are captured by the valency distribution, the filament length distribution and the distribution of direction cosines. Reconstituted collagen and fibrin networks have many features in common. Their filament length is log-normally distributed in the observed networks, but with a slightly higher normalized variance for the fibrin networks. This normalized variance does not show any density-dependence, but varies between biopolymer species (Table 1). Also, for both species, the node valency of the networks follows a shifted geometric distribution. The coordination number of the collagen networks are found in a narrow range $Z \in [3.38, 3.44]$, while fibrin has a lower and more spread coordination number $Z \in [3.19, 3.33]$. The orientation of filaments in the fibrin net-

works are correlated, indicating the presence of coherent fibers spanning multiple mesh sizes. These direction correlations are weaker for collagen, as indicated by a lower $\hat{B}$ (Table 1).

4.2 Infinitesimal strains

Infinitesimal macroscopic deformations are achieved by filament bending and torsion [12,23], leading to nonaffine node displacements [12,20]. Limiting the size of the network constrains these nonaffine deformations at the boundary, suggesting that the mechanical properties could be size-dependent. In rheology experiments, thin collagen discs in simple shear become stiffer as the sample thickness is decreased [32]. Our simulations confirm this size-dependence. Particularly, the shear modulus typically decreases with an increasing sample volume. The bulk modulus decreases with increasing sample volume for DBC boundary conditions but increases with increasing sample volume for IBC boundary conditions.

The Poisson's ratio ν of the network in its linear-elastic regime is defined by [45]

$$\nu = \frac{3K - 2G}{2(3K + G)}, \tag{9}$$

and thus inherit the dependence on size and boundary conditions from the shear and bulk moduli. The Poisson's ratio of 1.0 g/L collagen networks with $a/L = 80$ is $\nu = 0.36 \pm 0.01$, while that of 0.4 g/L fibrin networks is $\nu = 0.20 \pm 0.07$, where the error interval is the variability due to different boundary conditions.

Considering the simplifying assumption that all filaments have the same diameter and modulus, and considering that the average flexural rigidity of the filaments are associated with considerable uncertainty—only the order of magnitude could be established (Sec. 2.2)—the simulation prediction of the shear modulus is in fair agreement with rheological experiments.

4.3 Large strains

For simple shear deformations, strain-stiffening begins at a critical strain γ_c with an increase in the bending energy of the filaments. This is accompanied by a rapid increase in the elongational strain energy. Bending and stretching equipartition at a shear strain $\gamma_{eq} > \gamma_c$. For large strains $\gamma > \gamma_{eq}$, central force interactions dominate and networks become weakly strain-stiffening. Ultimately, the strain energy increases as γ^4, which is consistent with the large strain nonlinearity of simple shear. That is, no significant effect from the geometrical nonlinearity on the filament level is found. This can be explained by the fact that the greatest contribution to the response at larger strains comes from longitudinal deformation of the filaments, masking the stress-stiffening effect which would be manifested through filament bending.

The intermediate, strain stiffening regime $\gamma_c < \gamma < \gamma_{eq}$ is still dominated by so-called floppy modes of deformation, that is, mainly bending deformations invoking nonaffine displacements [12,25]. Beyond this regime $\gamma > \gamma_{eq}$, deformations are governed by filament stretching, and no network size-dependence is observed. This large strains regime observed in the simulations can thus be viewed as central-force interactions of linear springs. This theoretical picture for very large strains is, however, not in good agreement with rheology experiments for fibrin. Even though cross-linked fibrin has a linear force–deformation relation at least up to 120 % elongation [17], and we confirm that the elongation of individual filaments in the simulations is below 100 %, the strain-stiffening at large shear strains is remarkably overpredicted, as can be seen in Fig. 9b. This suggests a significant effect of deformation processes beyond the proposed theoretical frame of linear elastic filaments. One possibility is that irreversible damage is inflicted on the network, including fracture of filaments or branch-points, and possibly plastic deformation of filaments. A possible test of this hypothesis would be to conduct cyclic loading tests on the network.

Isotropic stretching of the network displays strain-stiffening similar to that of simple shear in the sense that a linear elastic regime, a strain-stiffening, bending-dominated regime, and a large-deformation, stretching-dominated regime can be observed. However, this occurs at relatively small deformations, so that the differential bulk modulus reaches a plateau already at about $\lambda - 1 = 0.05$. The strain-stiffening behavior of isotropic stretch has been previously attributed to the emergence of isostatic connectivity at a critical stretch [44], and our integrated differential bulk modulus is in qualitative agreement with previous simulations and a nonlinear mean-field model [44].

5 Conclusions

Both fibrin and collagen network geometries can be characterized statistically, in the sense that an inverse method can create network instances from the statistics, such that the large deformations mechanical response reproduces that of the physical networks. While network structures of collagen and fibrin are similar, the connectivity of fibrin is slightly lower, and the distribution of the filament length is wider. Moreover, the orientation of adjacent filaments are more correlated in fibrin, suggesting that coherent fibers significantly longer than the mesh size are present in the network.

While the density REV of biopolymers is about ten mesh sizes, the nonlocality of stresses, in conjunction with the heterogeneous microstructures, makes the stress REV of biopolymers very large, in the order of 10^2 mesh sizes. Therefore, the network characteristics near boundaries, in a composite structure or between membranes, differs significantly from the bulk

characteristics of the network. This may include the interior of the cell, narrow regions of healing (cuts), fibrosis and the basement membrane.

Small deformations, as well as the initial strain-stiffening, are governed by filament bending. Large strains are governed by filament stretching in the simulations and may be viewed as central-force interactions. However, simulations and experiments are not in good agreement for large strains, indicating that irreversible damage processes may be significant.

Acknowledgements

S.B.L. thanks BiMaC Innovation and the Alf de Ruvo Memorial Foundation of SCA AB for financial support. A.K. acknowledges the support of the WoodWisdom-net research program. This work was supported by the Harvard MRSEC (DMR-0820484) and NSF (DMR-1006546).

A Energy partition of the custom beam element

Consider a beam element and a Cartesian coordinate frame with the x direction along the length of a beam. The total elastic energy stored in a single beam element is computed as

$$U_{\mathrm{tot}} = \frac{1}{2}\mathbf{u}_{\mathrm{def}}^{\mathrm{T}}\mathbf{K}\mathbf{u}_{\mathrm{def}},$$

where $\mathbf{u}_{\mathrm{def}}$ is the displacement and $\mathbf{K}$ is the combined elastic and geometrical stiffness matrix. We separate this total energy into longitudinal tension/compression energy

$$U_\ell = \frac{1}{2}\int_0^{L_\mathrm{f}} \frac{F_x}{E_\mathrm{f}A}\mathrm{d}x,$$

bending energy

$$U_\mathrm{b} = \frac{1}{2}\left(\int_0^{L_\mathrm{f}} \frac{M_{xy}^2}{E_\mathrm{f}I_{xy}}\mathrm{d}x + \int_0^{L_\mathrm{f}} \frac{M_{xz}^2}{E_\mathrm{f}I_{xz}}\mathrm{d}x\right),$$

torsional energy

$$U_\mathrm{t} = \frac{1}{2}\int_0^{L_\mathrm{f}} \frac{T^2}{G_\mathrm{f}J}\mathrm{d}x$$

and the transverse shear energy

$$U_\mathrm{s} = U_{\mathrm{tot}} - U_\ell - U_\mathrm{b} - U_\mathrm{t},$$

where L_f is the length of the beam, F_x is the axial force in the beam, M_{xy} and M_{xz} are the bending moments with respect to the y and z axes, T is the torsional moment, E_f is the elastic modulus, G_f is the shear modulus, I_{xy} and I_{xz} are the geometrical moments of inertia with respect to the y and z axes and J is the polar moment of inertia. The cross-section area A is constant along the element, which, together with the assumed shape function, results in constant longitudinal force and torsional moment along the element and linearly varying bending moments.

References

1 G. Forgacs, S. A. Newman, B. Hinner, C. W. Maier and E. Sackmann, *Biophys. J.*, 2003, **84**, 1272–1280.
2 C. P. Brangwynne, G. H. Koenderink, E. Barry, Z. Dogic, F. C. MacKintosh and D. A. Weitz, *Biophys. J.*, 2007, **93**, 346–359.
3 J. E. Eriksson, T. Dechat, B. Grin, B. Helfand, M. Mendez, H.-M. Pallari and R. D. Goldman, *J. Clin. Inv.*, 2009, **119**, 1763–1771.
4 B. Furie and B. C. Furie, *Cell*, 1988, **53**, 505–518.
5 H. Lodish, A. Berk, S. L. Zipursky, P. Matsudaira, D. Baltimore and J. Darnell, *Molecular Cell Biology*, W. H. Freeman & Co. Ltd, 4th edn, 2000.
6 D. Vader, A. Kabla, D. Weitz and L. Mahadevan, *PLoS ONE*, 2009, **4**, e5902.
7 C. P. Broedersz, K. E. Kasza, L. M. Jawerth, S. Münster, D. A. Weitz and F. C. MacKintosh, *Soft Matter*, 2010, **6**, 4120–4127.
8 M. S. Sacks, *J. Elasticity*, 2000, **61**, 199246.
9 C. Storm, J. J. Pastore, F. C. MacKintosh, T. C. Lubensky and P. A. Janmey, *Nature*, 2005, **435**, 191–194.
10 F. C. MacKintosh, J. Kas and P. A. Janmey, *Phys. Rev. Lett.*, 1995, **75**, 4425–4428.
11 A. Kabla and L. Mahadevan, *J. R. Soc. Interface*, 2007, **4**, 99–106.
12 C. Heussinger, B. Schaefer and E. Frey, *Phys. Rev. E*, 2007, **76**, 031906.
13 C. Heussinger and E. Frey, *Phys. Rev. Lett.*, 2006, **97**, 105501.
14 M. Wyart, H. Liang, A. Kabla and L. Mahadevan, *Phys. Rev. Lett.*, 2008, **101**, 215501.
15 S. B. Lindström, D. A. Vader, A. Kulachenko and D. A. Weitz, *Phys. Rev. E*, 2010, **82**, 051905.
16 N. A. Kurniawan, S. Enemark and R. Rajagopalan, *J. Chem. Phys.*, 2012, **136**, 065101.
17 W. Liu, C. R. Carlisle, E. A. Sparks and M. Guthold, *J. Thromb. Haemost.*, 2010, **8**, 1030–1036.
18 Z. L. Shen, M. R. Dodge, H. Kahn, R. Ballarini and S. J. Eppell, *Biophys. J.*, 2008, **95**, 3956–3963.
19 M. J. Buehler, *J. Mech. Behav. Biomed. Mater.*, 2008, **1**, 59–67.
20 C. P. Broedersz, X. Mao, T. C. Lubensky and F. C. MacKintosh, *Nat. Phys.*, 2011, **7**, 983–988.
21 C. P. Broedersz, M. Sheinman and F. C. MacKintosh, *Phys. Rev. Lett.*, 2012, **108**, 078102.
22 S. Heyden, *PhD thesis*, LTH, Lund, Sweden, 2000.
23 P. R. Onck, T. Koeman, T. van Dillen and E. van der Giessen, *Phys. Rev. Lett.*, 2005, **95**, 178102.
24 E. M. Huisman, C. Storm and G. T. Barkema, *Phys. Rev. E*, 2008, **78**, 051801.
25 E. Conti and F. C. MacKintosh, *Phys. Rev. Lett.*, 2009, **102**, 088102.
26 H. Kang, Q. Wen, P. A. Janmey, J. X. Tang, E. Conti and F. C. MacKintosh, *J. Phys. Chem. B*, 2009, **113**, 3799–3805.
27 E. M. Huisman, T. van Dillen, P. R. Onck and E. Van der Giessen, *Phys. Rev. Lett.*, 2007, **99**, 208103.
28 E. Kim, O. V. Kim, K. R. Machlus, X. Liu, T. Kupaev, J. Lioi, A. S. Wolberg, D. Z. Chen, E. D. Rosen, Z. Xua and M. Alber, *Soft Matter*, 2011, **7**, 4983–4992.

29 P. K. Purohit, R. I. Litvinov, A. E. Brown, D. E. Discher and J. W. Weisel, *Acta Biomater.*, 2011, **7**, 2374–2383.
30 A. M. Stein, D. A. Vader, D. A. Weitz and L. M. Sander, *Complexity*, 2011, 22–28.
31 A. M. Stein, D. A. Vader, L. M. Jawerth, D. A. Weitz and L. M. Sander, *J. Microscopy*, 2008, **232**, 463–475.
32 R. C. Arevalo, J. S. Urbach and D. L. Blair, *Biophys. J.*, 2010, **99**, 65–67.
33 A. Baici, G. Cohen, K. Fehr and A. Böni, *Anal. Biochem.*, 1980, **108**, 230–232.
34 D. A. Vader, *PhD thesis*, Harvard University, 2010.
35 M. Guthold, W. Liu, B. J. Stephens, S. T. Lord, R. R. Hantgan, D. A. Erie, R. M. Taylor and R. Superfine, *Biophys. J.*, 2004, **87**, 4226–4236.
36 W. Liu, L. M. Jawerth, E. A. Sparks, M. R. Falvo, R. R. Hantgan, R. Superfine, S. T. Lord and M. Guthold, *Science*, 2006, **313**, 634.
37 J. C. Maxwell, *Phil. Mag.*, 1864, **27**, 294–299.
38 M. F. Thorpe, *J. Non-Cryst. Solids*, 1983, **57**, 355–370.
39 ANSYS, in *Theory Reference for the Mechanical APDL and Mechanical Applications*, ed. P. Kohnke, Ansys Inc., Southpointe, US, 2012.
40 J. S. Przemieniecki, *Theory of Matrix Structural Analysis*, McGraw-Hill Book Company., 1968.
41 C. C. Rankin and F. A. Brogan, *J. Press. Vess.-T. ASME*, 1986, **108**, 165–174.
42 C. C. Rankin and B. Nour-Omid, *Comput. Struct.*, 1988, **30**, 257–267.
43 B. Nour-Omid and C. C. Rankin, *Comput. Method. Appl. M.*, 1991, **93**, 353–384.
44 M. Sheinman, C. P. Broedersz and F. C. MacKintosh, *Phys. Rev. E*, 2012, **85**, 021801.
45 Y. C. Fung and P. Tong, in *Classical and computational solid mechanics*, World scientific, 2001, vol. 1.